

# Assignment 5: Eigenvalue problems with B-splines

Marta Casado Carrasquer

May 6, 2025

## 1 Introduction

The hydrogen atom is one of the few quantum systems that is analytically solvable. In this project, we aim to numerically solve the radial Schrödinger equation for hydrogen-like ions using B-splines.

We discretize the Schrödinger equation in order to obtain a generalized eigenvalue problem, explore different types of knot sequences, use Gaussian quadrature for numerical integration and compare the numerical results to the analytical solutions. Furthermore, we investigate how our results are affected when the nuclear potential is modified to model a uniformly charged sphere, both for hydrogen and heavy nuclei such as uranium.

## 2 Theory and Methods

### 2.1 Radial Schrödinger Equation in Hartree Units

The objective is to numerically solve the radial Schrödinger equation for hydrogen-like ions in Hartree atomic units. Writing the radial function as  $P_{n\ell}(r)$  (where  $P_{n\ell}(r) = r R_{n\ell}(r)$ ), the one-dimensional equation reads:

$$-\frac{1}{2} \frac{d^2 P_{n\ell}(r)}{dr^2} + \left[ \frac{\ell(\ell+1)}{2r^2} + V(r) \right] P_{n\ell}(r) = E P_{n\ell}(r) \quad (1)$$

where  $\ell$  is the angular momentum quantum number.

## 2.2 B-splines and Knot Sequence

We want to expand the radial function using B-spline basis functions of degree  $p$ :

$$P_{n\ell}(r) = \sum_i c_i B_{i,k}(r). \quad (2)$$

which we define over a knot sequence of choice. The sequences are created as follows:

1. **Linear Knot Sequence:** We create a set of equidistant points from  $r = 0$  to some cut-off  $r_{\text{cut}}$ . This allows us to capture the rapid change of the wave function near the origin.
2. **Exponential or Quadratic Knot Sequence:** Once reached our cut-off radius  $r_{\text{cut}}$ , the wave function changes more slowly. Therefore, we use an exponential or quadratic spacing from  $[r_{\text{cut}}, r_{\text{max}}]$  since less points are needed in order to describe this region.

Exponential set:

$$r_{\text{exp}} = r_{\text{cut}} + (r_{\text{max}} - r_{\text{cut}}) \frac{\exp(s) - 1}{\exp(1) - 1}$$

Quadratic set:

$$r_{\text{quad}} = r_{\text{cut}} + s^2(r_{\text{max}} - r_{\text{cut}})$$

where  $s$  is a uniformly sampled point between 0 and 1. Note that we have also kept the option to apply a linear set after  $r_{\text{cut}}$ .

3. **Full Knot Sequence:** The full sequence is created by concatenating the linear set before  $r_{\text{cut}}$  with the chosen sequence after  $r_{\text{cut}}$ . To enforce the boundary conditions (i.e., ensuring the trial function vanishes at  $r = 0$  and  $r = R_{\text{max}}$ ), the first and last knot positions are repeated  $k$  times (where  $k$  is the order of the B-spline). This augmentation both facilitates the proper behavior of the basis functions at the endpoints and guarantees that only interior basis functions contribute to the solution.

## 2.3 Matrix Representation

After representing the radial function using B-splines, we insert our ansatz into the Schrödinger equation yielding the following generalized eigenvalue problem:

$$\mathbf{H}\mathbf{c} = E\mathbf{B}\mathbf{c} \quad (3)$$

where  $\mathbf{B}$  has the form:

$$B_{ij} = \int_0^{r_{\max}} B_{i,k}(r) B_{j,k}(r) dr \quad (4)$$

and the Hamiltonian matrix  $\mathbf{H}$  is:

$$H_{ij} = \frac{1}{2} \int_0^{r_{\max}} \frac{dB_{i,k}(r)}{dr} \frac{dB_{j,k}(r)}{dr} dr + \int_0^{r_{\max}} \left[ \frac{\ell(\ell+1)}{2r^2} + V(r) \right] B_{i,k}(r) B_{j,k}(r) dr \quad (5)$$

We solve the problem using the `eigh` function from the SciPy library so we are able to find the eigenvalues  $E$ , which correspond to the energy levels, and the eigenvectors  $\mathbf{c}$  which define the wave functions in the B-spline basis.

## 2.4 Imposing Boundary Conditions

Before reconstructing our radial wave function, we need to impose some boundary conditions:

$$P_{n\ell}(0) = 0 \quad (6)$$

$$P_{n\ell}(r \rightarrow r_{\max}) \rightarrow 0 \quad (7)$$

In order to do so, we repeat the first and last knots of our full knot sequence  $p$  times. This ensures that the only non-zero contributions near the boundaries come from the first and last B-splines. By simply removing these basis functions (reducing  $\mathbf{H}$  and  $\mathbf{B}$ ), the boundary conditions are fulfilled. After solving the generalized eigenvalue problem (3), the full coefficient set is reconstructed by setting the eliminated coefficients to zero. Once  $\mathbf{c}$  are obtained, we can reconstruct the radial wave function (2).

## 2.5 Numerical Integration using Gaussian Quadrature

The integrals in Eqs. (4) and (5) are computed using Gaussian quadrature. The integral of a function  $f(r)$  is approximated in each subinterval  $[t_i, t_{i+1}]$  (defined by our unaugmented full knot sequence) by the following formula

$$\int_{t_i}^{t_{i+1}} f(r) dr \approx \sum_{j=1}^{n_{\text{quad}}} w_j f(x_j) \quad (8)$$

where  $n_{\text{quad}}$  is the number of quadrature points used and the abscissas  $x_j$  and weights  $w_j$  are defined for the interval  $[-1, 1]$ . Therefore, we apply a mapping in order to transform the abscissas and weights from  $[-1, 1]$  to  $[t_i, t_{i+1}]$ .

We make the substitution:

$$r = \frac{t_{i+1} - t_i}{2} x + \frac{t_{i+1} + t_i}{2} \quad (9)$$

and:

$$dr = \frac{t_{i+1} - t_i}{2} dx \quad (10)$$

Which yields:

$$\int_{t_i}^{t_{i+1}} f(r) dr = \frac{t_{i+1} - t_i}{2} \int_{-1}^1 f\left(\frac{t_{i+1} - t_i}{2} x + \frac{t_{i+1} + t_i}{2}\right) dx \quad (11)$$

Applying the Gauss-Legendre quadrature, we obtain:

$$\int_{t_i}^{t_{i+1}} f(r) dr \approx \frac{t_{i+1} - t_i}{2} \sum_{j=1}^{n_{\text{quad}}} w_j f\left(\frac{t_{i+1} - t_i}{2} x_j + \frac{t_{i+1} + t_i}{2}\right) \quad (12)$$

## 2.6 Potentials Models

We use two different potentials:

**Coulomb Potential:** For a point-charge nucleus, the potential in Hartree units is given by:

$$V(r) = -\frac{Z}{r} \quad (13)$$

where  $Z$  is the nuclear charge. We can solve this potential analytically for the energy levels as:

$$E_n = -\frac{Z^2}{2n^2} \quad (14)$$

and for the radial wave functions:

$$P_{nl}(r) = rR_{nl}(r) = rN_{nl} \left(\frac{2Zr}{n}\right)^l e^{-Zr/n} L_{n-l-1}^{2l+1}\left(\frac{2Zr}{n}\right) \quad (15)$$

where  $N_{nl}$  is the normalization constant,  $L_{n-l-1}^{2l+1}$  are the associated Laguerre polynomials and  $n$  is the principal quantum number.

**Spherical Uniformly Charged Potential:** For a finite-size nucleus, the potential in Hartree units is given by:

$$V(r) = \begin{cases} -\frac{Z}{r}, & r \geq R_0 \\ -Z \left( \frac{3}{2R_0} - \frac{r^2}{2R_0^3} \right), & r < R_0 \end{cases} \quad (16)$$

where  $R_0$  represents the nuclear radius. We apply it for two cases:

- **Hydrogen:** with a small radius  $R_0 = 1.5$  Bohr radii, for a few angular momenta.
- **Uranium-238:** with  $Z = 92$  and  $R_0 = 1.2A^{1/3}$  fm, where  $A = 238$ , converted to Hartree units.

### 3 Results and Discussion

#### 3.1 Knot Sequences: Linear, Exponential, and Quadratic

B-splines of degree  $p = 4$  were used. Here we present examples of how the spacing between knots for our different knot sequences looks like as well as their corresponding B-spline basis functions.

- **Linear:**

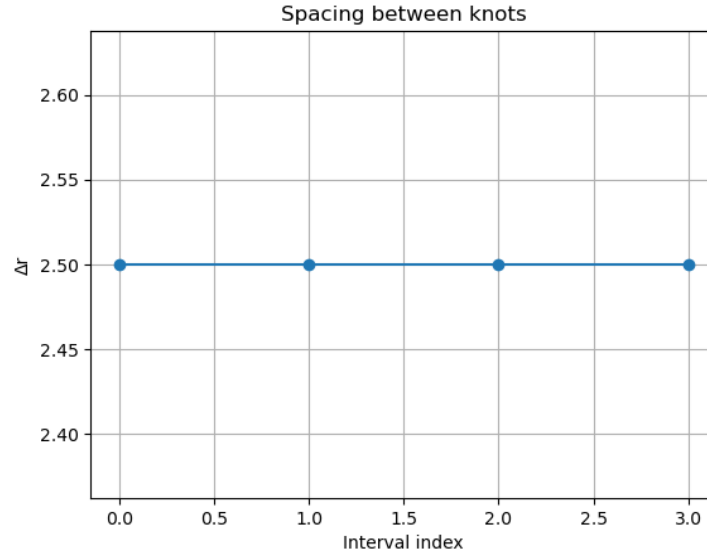


Figure 1: Spacing  $\Delta r$  between knots for the linear scheme.

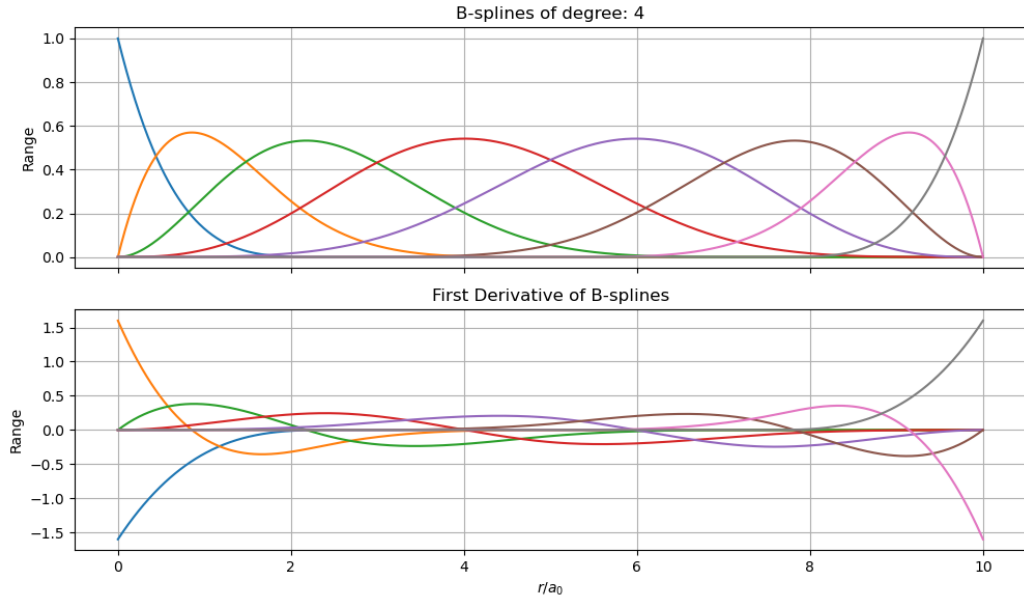


Figure 2: B-spline basis functions and their first derivatives for the linear scheme.

- **Exponential:**

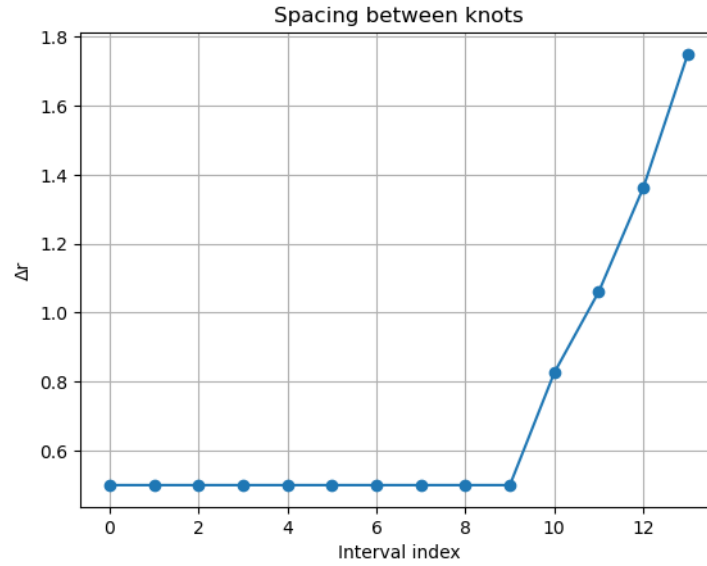


Figure 3: Spacing  $\Delta r$  between knots for the exponential scheme with 10 knots before  $r_{\text{cut}}$  and 5 knots after.

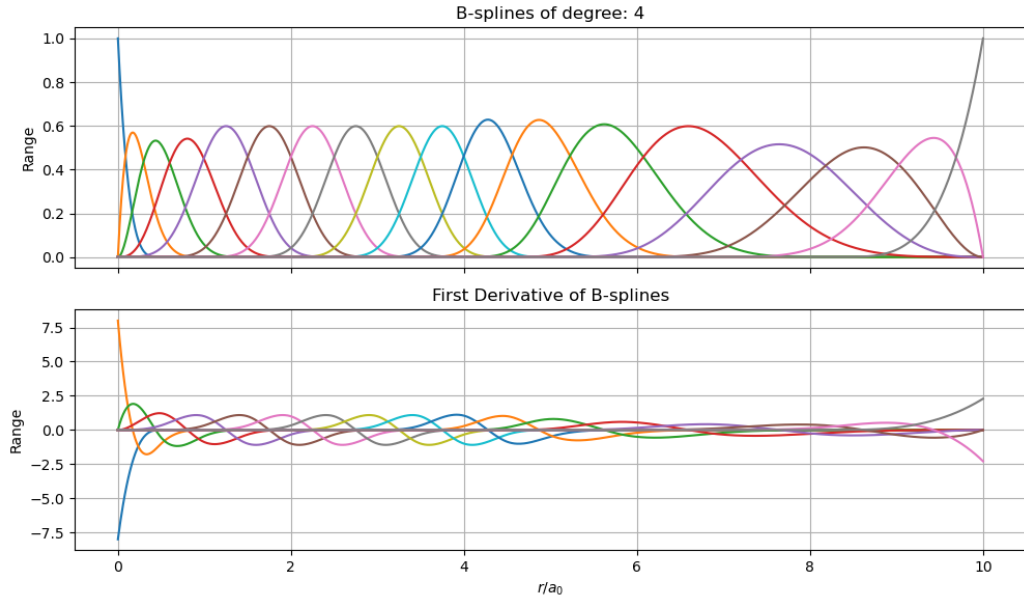


Figure 4: B-spline basis functions and their first derivatives for the exponential scheme.

- Quadratic:

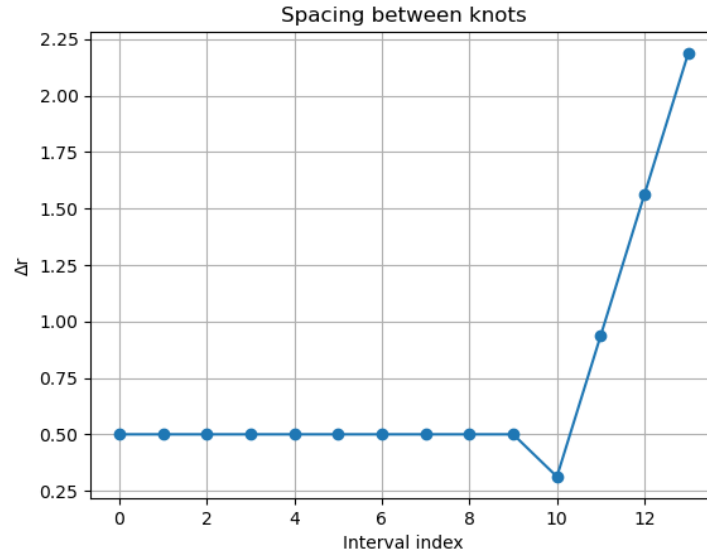


Figure 5: Spacing  $\Delta r$  between knots for the quadratic scheme with 10 knots before  $r_{\text{cut}}$  and 5 knots after.

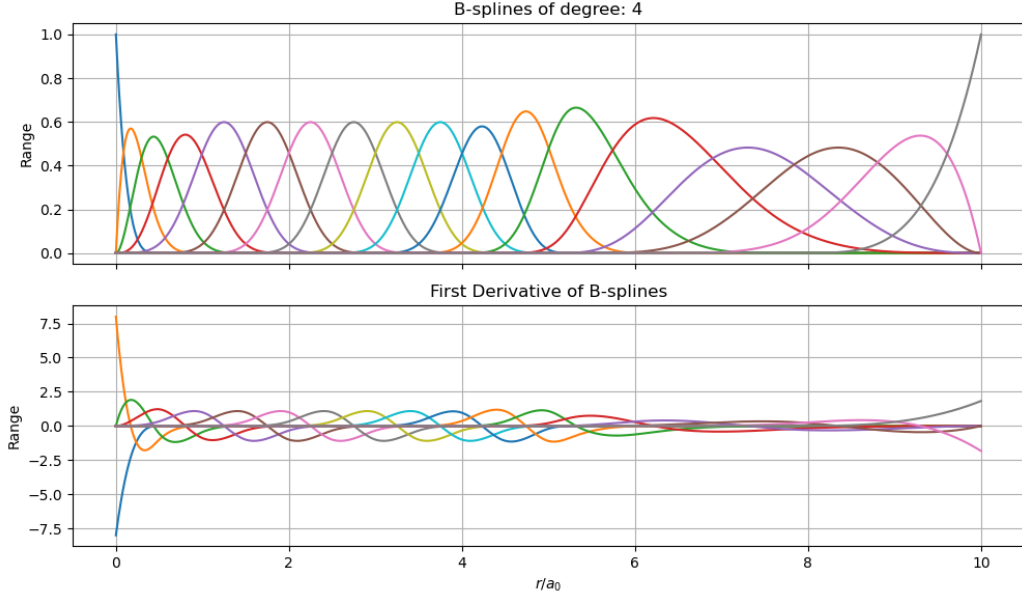


Figure 6: B-spline basis functions and their first derivatives for the quadratic scheme.

As observed from the figures above, the linear scheme has a uniform step size which can be inefficient far from the origin. The exponential and quadratic schemes allow for a denser knot clustering before  $r_{\text{cut}}$  and a more widely spaced knot sequence in the outer region, which are suitable approaches for fast decaying wave functions.

When observing the B-splines and their first derivatives, we see how the different knot sequences influence the shape and localization of the basis functions.

### 3.2 Convergence of Gaussian Quadrature

To ensure accurate integration, we test the convergence of the Gaussian quadrature used to compute the overlap matrix  $\mathbf{B}$ . We compute the norm of the matrix for different numbers of quadrature points  $n_{\text{quad}}$ .



$n_{\text{quad}}$	$\ \mathbf{B}\ $
3	6.165889
5	6.171421
7	6.171421
10	6.171421

Table 1: Norm of matrix  $\mathbf{B}$  for different values of  $n_{\text{quad}}$ .

As seen in Table 1, the norm converges rapidly with  $n_{\text{quad}}$ . A value of  $n_{\text{quad}} = 5$  is good enough for an accurate integration.

### 3.3 Coulomb Potential and Analytical Comparison

All three knot sequences yield accurate results for the hydrogen atom using a Coulomb potential. However, the linear scheme needs a larger number of knots to achieve the same accuracy as the other two sequences. Therefore, we choose the exponential scheme for the rest of the calculations, since it yields the lowest error.

We compare our numerical implementation with the known analytical values.

#### 3.3.1 Results for $\ell = 0$

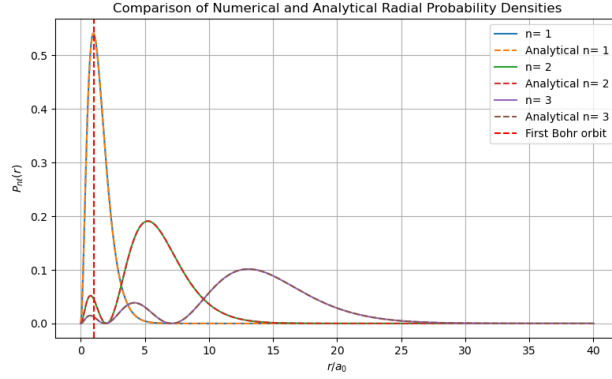


Figure 7: First three states radial probability densities comparison for  $\ell = 0$  with 10 knots before  $r_{\text{cut}} = 15$  and 5 knots after.

$n$	Numerical	Analytical	$\Delta E$
1	-0.499932	-0.500000 Ha	6.84e-05 Ha
2	-0.124998 Ha	-0.125000 Ha	2.21e-06 Ha
3	-0.055554 Ha	-0.055556 Ha	1.82e-06 Ha

Table 2: Comparison of numerical and analytical eigenvalues for  $\ell = 0$ .

### 3.3.2 Results for $\ell = 1$

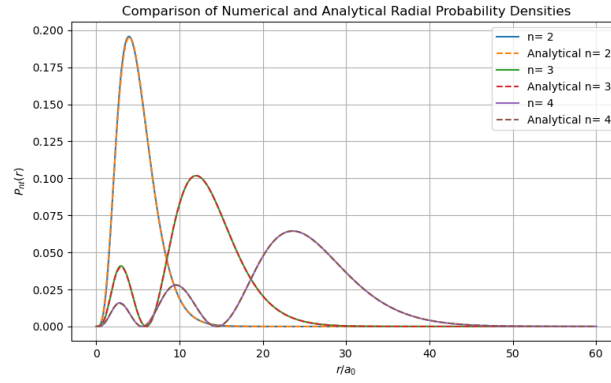


Figure 8: First three states radial probability densities comparison for  $\ell = 1$  with 10 knots before  $r_{\text{cut}} = 30$  and 5 knots after.

$n$	Numerical	Analytical	$\Delta E$
2	-0.124889 Ha	-0.125000 Ha	1.11e-04 Ha
3	-0.055527 Ha	-0.055556 Ha	2.89e-05 Ha
4	-0.031237 Ha	-0.031250 Ha	1.27e-05 Ha

Table 3: Comparison of numerical and analytical eigenvalues for  $\ell = 1$  Coulomb potential.

### 3.3.3 Results for $\ell = 2$

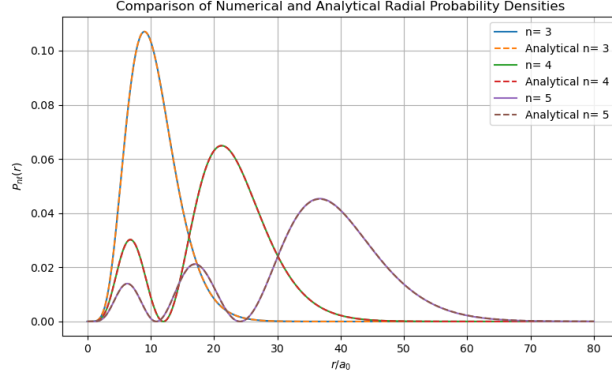


Figure 9: First three states radial probability densities comparison for  $\ell = 2$  with 10 knots before  $r_{\text{cut}} = 30$  and 5 knots after.

$n$	Numerical	Analytical	$\Delta E$
3	-0.055552 Ha	-0.055556 Ha	3.54e-06 Ha
4	-0.031248 Ha	-0.031250 Ha	2.18e-06 Ha
5	-0.019996 Ha	-0.020000 Ha	3.98e-06 Ha

Table 4: Comparison of numerical and analytical eigenvalues for  $\ell = 2$ .

As seen in the figures and tables above, our numerical implementation is in great agreement with the analytical solutions for the hydrogen atom for different values of  $\ell$ . Beyond matching the energy values quantitatively, we also recover the correct ordering of states. Since the principal quantum number must satisfy  $n > \ell$ , the lowest energy state for a given  $\ell$  corresponds to  $n = \ell + 1$ . Therefore, the first energy level for  $\ell = 1$  should match the second energy level for  $\ell = 0$ , and this pattern should continue for higher  $\ell$ . This correspondence is indeed observed in our numerical results.

## 3.4 Orbital Visualization

In order to visualize the orbitals for the s-states under the Coulomb potential, we construct a 2D heatmap of the radial probability density  $P(r) = r^2|R(r)|^2$ .

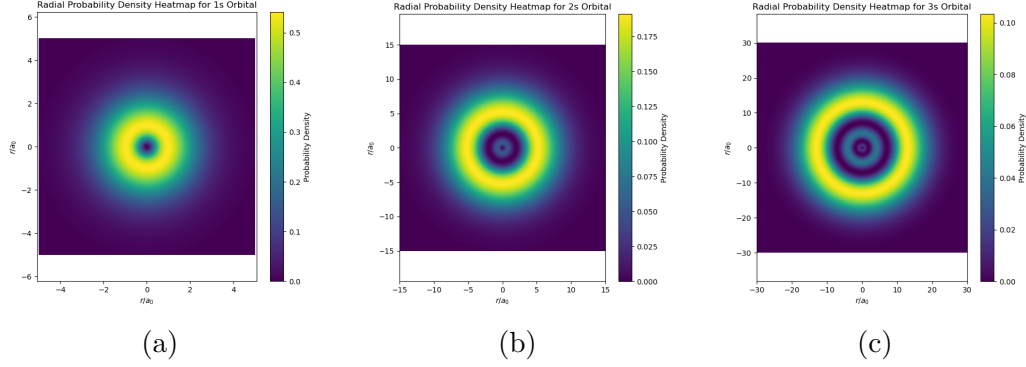


Figure 10: 2D heatmaps of the radial probability densities for orbitals: 1s, 2s and 3s.

From Figure 10 we can clearly see an empty centre in each heatmap, this reflects the fact that the radial probability density satisfies the boundary condition  $P(0) = 0$ . Furthermore, as observed in the previous section, the higher the energy level, the larger the radial extent of the orbital. This means that for excited states, we need to increase our domain to properly visualize the probability density.

### 3.5 Spherically Uniformly Charged Potential

We now replace the Coulomb potential with a spherically uniformly charged nuclear potential.

### 3.5.1 Uranium Potential

For uranium ( $Z = 92$ ), we obtain the following:

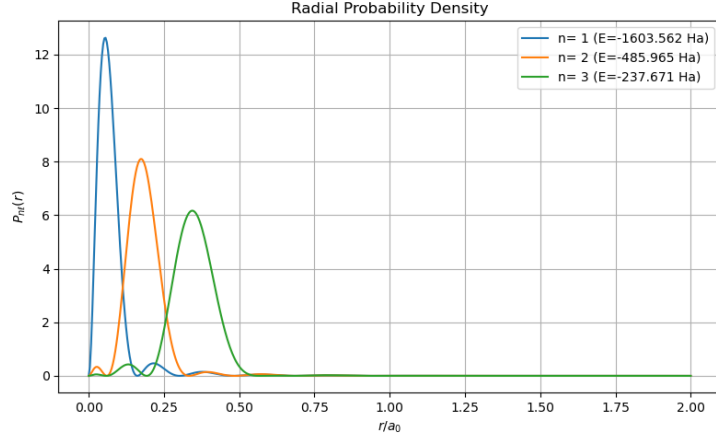


Figure 11: First three states radial probability densities for uranium ( $Z = 92$ ) when  $\ell = 0$  with 5 knots before  $r_{\text{cut}} = 1$  and 2 knots after.

The radial probability densities  $P_{n\ell}(r)$  for uranium show differences compared to hydrogen system with  $Z = 1$  studied in sections above. We observe how the eigenvalues are much more negative than for hydrogen. Moreover, the probability densities are highly localized near the nucleus which made us reduce our domain significantly compared to hydrogen. As the principal quantum number  $n$  increases, the peak positions shift outward, though they remain much closer to the nucleus than in hydrogen.

### 3.5.2 Small Radius $R_0$

We also compare the Coulomb case with a spherical charge distribution in a sphere of  $R_0 = 1.5$  Bohr radii, both with  $Z = 1$ , for a few angular momenta and obtain the following results:

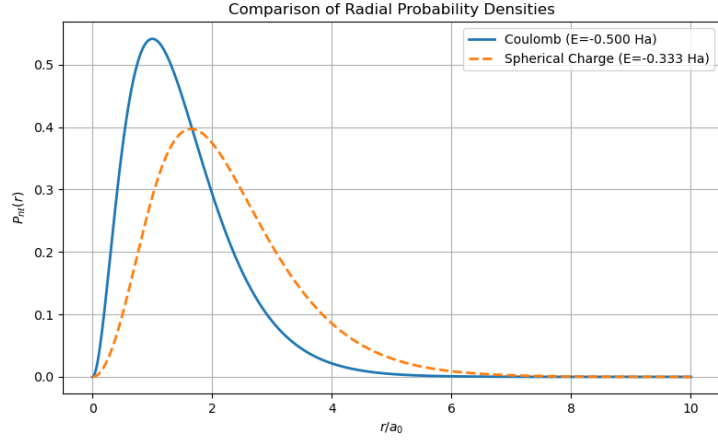


Figure 12: Comparison between Coulomb and spherical charge case for  $\ell = 0$  with 10 knots before  $r_{\text{cut}} = 5$  and 5 knots after.

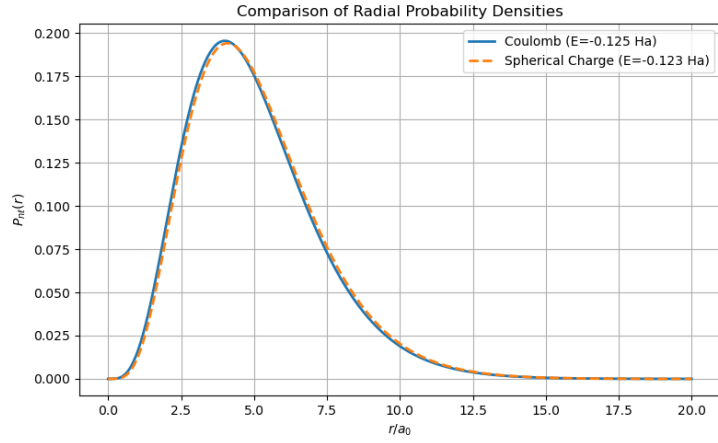


Figure 13: Comparison between Coulomb and spherical charge case for  $\ell = 1$  with 15 knots before  $r_{\text{cut}} = 10$  and 5 knots after.

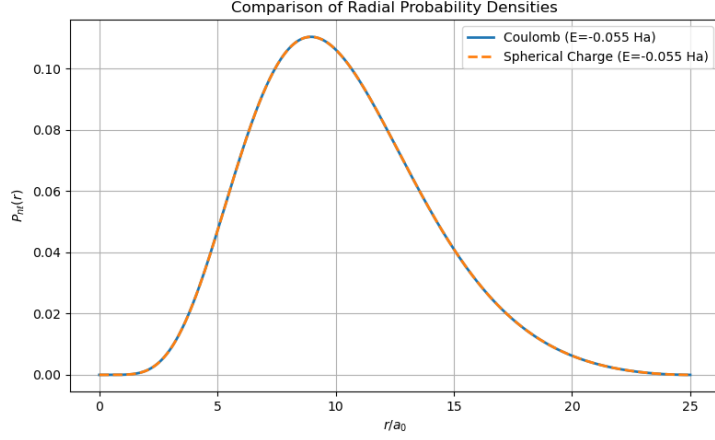


Figure 14: Comparison between Coulomb and spherical charge case for  $\ell = 2$  with 10 knots before  $r_{\text{cut}} = 15$  and 5 knots after.

As seen in the figures, we observe a clear trend as the angular momentum quantum number  $\ell$  increases. For  $\ell = 0$ , the eigenvalue obtained using the spherical charge distribution is less negative than that of the Coulomb case. This is clearly visible in both the energy values and in the shift in the radial probability density peak. As we increase to  $\ell = 1$ , the difference between the two potentials becomes much smaller, with the eigenvalues and probability densities closely aligned. Finally, for  $\ell = 2$ , the eigenvalues from both potentials match perfectly and their radial probability densities are indistinguishable.

## 4 Conclusions

Our numerical implementation was validated against analytical solutions for the Coulomb potential, yielding eigenvalues and wave functions with great agreement for various angular momentum quantum numbers  $\ell$ . We also found that an exponential knot sequence offered the most efficient resolution. Lastly, we explored the effects of modelling the nucleus as a uniformly charged sphere. From our results, we demonstrated the reliability and flexibility of our numerical implementation.